Simulations of granular bed erosion due to laminar shear flow near the critical Shields number

J. J. Derksen

Citation: Phys. Fluids **23**, 113303 (2011); doi: 10.1063/1.3660258
View online: http://dx.doi.org/10.1063/1.3660258
View Table of Contents: http://pof.aip.org/resource/1/PHFLE6/v23/i11
Published by the American Institute of Physics.

Simulations of granular bed erosion due to laminar shear flow near the critical Shields number

J. J. Derksen[a)]
Chemical & Materials Engineering, University of Alberta, Edmonton, Alberta T6G 2G6, Canada

(Received 24 May 2011; accepted 20 October 2011; published online 17 November 2011)

Direct numerical simulations of granular beds consisting of uniformly sized spherical particles being eroded by a shear flow of Newtonian liquid have been performed. The lattice-Boltzmann method has been used for resolving the flow of the interstitial liquid. Fluid and solid dynamics are fully coupled with the particles having finite size and undergoing hard-sphere collisions. Only laminar flow has been considered with particle-based Reynolds numbers in the range 0.02 to 0.6. The parameter range of the simulations covers the transition between static and mobilized beds. The transition occurs for $0.10 < \theta < 0.15$ with θ the Shields number. The transition is insensitive of the Reynolds number and the solid-over-liquid density ratio. Incipient bed motion has been interpreted in terms of the probability density functions of the hydrodynamic forces acting on the spheres in the upper layer of the bed. © *2011 American Institute of Physics*.
[doi:10.1063/1.3660258]

I. INTRODUCTION

Erosion of granular beds by a fluid flow occurs in many natural and engineered situations: wind blowing over desert sand, tidal flows interacting with sea beds and beaches, flows in horizontal or slightly inclined slurry pipelines that have a deposit layer of granular material, mixing tanks containing an incompletely suspended slurry. The granular bed and the flow interact, and the nature and extent of the interactions depend on the flow characteristics, fluid properties, and bed properties such as its density, topology, particle size and shape distributions, and inter-particle forces. In the majority of applications the fluid flow over the bed is turbulent which makes bed erosion a complicated, multi-scale process. The turbulent flow over the bed has a spectrum of length scales interacting with the bed. Once detached from the bed the suspended particles feel this multitude of flow scales that eventually determine the fate of the particles: getting transported away from the bed or falling back into it again.

In this paper, however, for a number of reasons the focus is on granular beds eroded by laminar flow: In the first place because we are interested in fine particles forming macroscopically flat beds so that Reynolds numbers based on particle size are relatively small and the relevant two-phase flow phenomena take place in the viscous part of the boundary layer above the bed. In the second place because we want to identify the fundamental mechanisms and phenomena critical to bed erosion for relatively simple systems first, before embarking on much more complicated turbulent cases. In the third place because of the availability of detailed experimental data on erosion due to laminar shear flow in well-defined systems.[1–5] The present study is purely computational. Numerical simulations allow for looking into erosion mechanisms in detail and reveal information difficult to come by through experimentation (e.g., because of limited optical accessibility). Simulations also make it possible to check sensitivities of erosion processes with respect to flow conditions, bed properties, and physical phenomena (e.g., interparticle forces can be switched on and off at will). At the same time experimental data are needed to guide the computational approach and assess the level of realism achieved in simulations.

As noted above, important experimental papers on granular bed erosion as a result of laminar shear are due to Charru and co-workers.[1,2,4] In addition, papers due to Lobkovsky *et al.*,[3] Ouriemi *et al.*,[5] and Loiseleux *et al.*[6] provide valuable insights. The broader topic of critical Shields numbers has received much attention, specifically in the context of civil engineering (e.g., the review due to Buffington and Montgomery,[7] and Paphitis[8]). The Shields number θ is the ratio of shear stress over net gravity: $\theta \equiv \frac{\rho\nu\dot{\gamma}}{g(\rho_p-\rho)2a}$ (with ν and ρ the kinematic viscosity and density of the Newtonian fluid, ρ_p and a the particle density and radius, $\dot{\gamma}$ the shear rate experienced by the upper layer of the bed, and g gravitational acceleration) and is widely used to characterize sheared granular beds. The critical Shields number θ_c is the demarcation between static (non-eroded) and dynamic beds (beds being eroded).

At the critical Shields number incipient bed erosion occurs. It has been suggested[5] that the critical Shields number is independent of the particle-based Reynolds number ($\mathrm{Re} \equiv \frac{a^2\dot{\gamma}}{\nu}$) in a wide range of (low to moderate) Reynolds numbers. This would imply that viscous forces, not inertial (lift) forces are responsible for incipient erosion: In order for particles (here and in the rest of the paper we assume particles to be solid spheres with radius a) in the upper layer of the bed to start moving, the flow must provide vertical forces that overcome the net gravity force acting on the particle: $F_{vert} \geq \frac{4\pi}{3}a^3 g(\rho_p - \rho)$. A vertical force due to viscous effects would scale according to $F_{vert} = C_1\rho\nu\dot{\gamma}a^2$, a vertical force due to inertial lift according to $F_{vert} = C_2\rho\dot{\gamma}^2a^4$ [9,10]

[a)]Electronic mail: jos@ualberta.ca.

with C_1 and C_2 dimensionless proportionality constants of the order 1−10. Only in case the vertical force is viscous, the force inequality can be written in terms of a constant (i.e., Re-independent) critical Shields number: $\frac{\nu\rho\dot{\gamma}}{g(\rho_p-\rho)2a} \geq \frac{4\pi}{3}\frac{1}{2C_1}$ and $\frac{4\pi}{3}\frac{1}{2C_1}$ can thus be interpreted as the critical Shields number. In recent work,[10] we have shown that the vertical forces due to a simple shear flow acting on spheres in the upper layer of a granular bed are dominated by the sphere-to-sphere force variation, not by the vertical force averaged over all spheres in the upper layer. While the average vertical force scales according to inertial lift, the sphere-to-sphere variation of the vertical force (in that paper quantified by the root-mean-square value) scales as viscous drag. The distribution of vertical forces experienced by individual spheres is very wide. In terms of the constant C_1, peak forces reach levels so that C_1 gets of the order of 10. Since the critical Shields number relates to incipient bed erosion, the peak force levels matter for θ_c (not so much the averages), so that the critical Shields number $\frac{4\pi}{3}\frac{1}{2C_1}$ would be of the order 0.2. This is a value in order-of-magnitude agreement with experimental data.[5,6]

In this paper, we describe three-dimensional, time-dependent numerical simulations of the joint motion of Newtonian fluid and uniformly sized spherical particles. Next to hydrodynamic forces, the solid spheres feel gravity and they undergo hard-sphere collisions with neighboring spheres. The spheres form a dense bed that is supported by a flat, horizontally placed wall. An opposing wall placed well above the particle bed moves horizontally and thereby creates a shear flow in the liquid above the bed. In our numerical simulations we attempt as much as possible to resolve the motion of liquid and particles. The flow of liquid above and in the bed is simulated with the lattice-Boltzmann method (LBM).[11,12] The no-slip condition at the surfaces of the (translating and rotating) particles is achieved by an immersed boundary method.[13,14] The spatial resolution of the simulations is such that the particle radius a spans 6 spacings on the uniform and cubic lattice as used in the simulations. The lattice-Boltzmann method provides the hydrodynamic forces and torques acting on each individual particle. These are used (according to Newton's second law) to update the linear and angular velocities and the positions of the particles that in turn provide the boundary conditions for the liquid flow. In the simulations this tightly coupled solid-liquid system is evolved in time. Two-dimensional simulations (with circular disks instead of spheres) of similar systems have been reported by Papista *et al.*[15] While providing interesting insights, the predictive capability of 2D simulations is limited given the inherently three-dimensional nature of the flow through and above 3D assemblies of spherical particles.

In parts of the flow domain the solids form a dense suspension with closely spaced spheres. On the fixed grid that is used, this implies that the interstitial liquid flow is locally not fully resolved. To compensate for this, radial lubrication forces (according to low-Reynolds number analytical expressions[16]) are explicitly added to the equations of motion of the particles. The sensitivity of this modeling step on the bed dynamics has been investigated in this paper. Similarly the role of the dry (sphere-sphere) contact parameters (more specifically the friction coefficient which represents the effect of unresolved surface roughness) needs attention.

The goals of this paper are (1) to outline a methodology for performing direct simulations with resolution of the solid-liquid interfaces of sheared granular beds; (2) to investigate if the simulations capture phenomena as observed in experimental studies; (3) to use the detailed information generated in the simulations to try and identify key mechanisms in the mobilization of solids in sheared granular beds.

The paper is organized in the following manner: In Sec. II, the flow systems are defined and dimensionless numbers that make up the parameter space are identified. We distinguish between physical dimensionless numbers on one side and dimensionless numbers related to the numerical process and/or related to modeling assumptions on the other. Then the numerical procedure is described. In Sec. IV, first some impressions of main flow features are presented, followed by an account of the impact of numerical and modeling settings on bed mobility. We then study the effects of the Shields and the Reynolds number. These effects are interpreted by assessing hydrodynamic forces experienced by the particles. In Sec. V, we summarize and reiterate the main conclusions.

II. FLOW SYSTEMS

The basic flow configuration with a Cartesian coordinate system is sketched in Figure 1: we have a flat wall of size $L \times W$ supporting a bed of spherical particles all having the same radius a. The bed consists of a dense monolayer of immobile spheres glued to the bottom wall on top of which there is a layer of mobile spheres of typically $8a$ thickness. The surface fraction of the immobile bottom layer is $\sigma \equiv n\pi a^2 \approx 0.7$ with n the number of spheres per unit area. The spheres in the bottom layer are placed such that they all touch the flat bottom wall. The mobile layers of spheres on top are generated by randomly placing spheres above the bottom layer. These spheres we let fall through vacuum towards the bottom layer where non-elastic sphere-sphere collisions (restitution coefficient $e = 0.8$) remove the energy from this granular system so that it eventually comes to rest. We then end up with a fairly loosely packed bed with overall solids volume fraction $\phi \approx 0.52$. Note that ϕ is also limited because the bed is relatively shallow and bounded by a flat

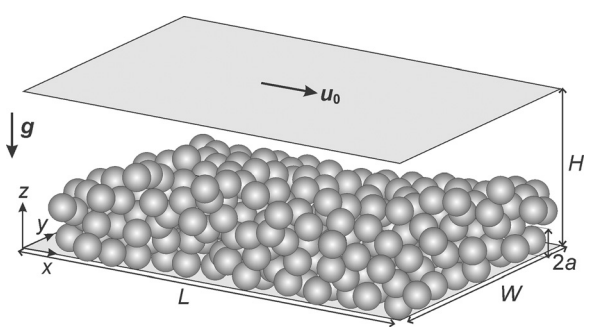

FIG. 1. Flow geometry and coordinate system. Randomly placed spheres on the flat bottom wall experience a shear flow due to the motion in x-direction of an upper wall.

wall below and a free surface at the top. In the process of making the granular bed, periodic conditions in x and y-direction apply.

After the bed has been formed, the void space and the space above the granular bed is filled with liquid to a level $z=H$ above the bottom plate. A shear flow of the liquid is generated by placing a wall parallel to the bottom wall at vertical distance H and giving that wall a velocity u_0 in the positive x-direction (see Figure 1). The overall shear rate experienced by the bed of spheres $\dot{\gamma}_0$ depends on u_0 and the height of the open space above the bed. The latter—in turn—depends on to what extent the shear flow is able to expand and/or erode the bed and suspend particles in the liquid above the bed. As a consequence $\dot{\gamma}_0$ is a result, not an input parameter of the simulations. In this work $\dot{\gamma}_0$ is calculated for each simulation separately by determining—once the flow is stationary—the average liquid velocity $\langle u_x \rangle$ as a function of z inside and above the bed and taking the derivative of the linear portion of this profile well above the bed (see below for examples): $\dot{\gamma}_0 = \frac{d\langle u_x \rangle}{dz}$. This overall shear rate we use in the definitions of the (particle-based) Reynolds number and Shields number, $\mathrm{Re} = \frac{\dot{\gamma}_0 a^2}{\nu}$ and $\theta = \frac{\rho \nu \dot{\gamma}_0}{g(\rho_p - \rho)2a}$, respectively. As a third independent dimensionless number that governs this flow system the density ratio $\frac{\rho_p}{\rho}$ is taken. Note that, e.g., a Stokes number can be defined by combining Re and the density ratio: $\mathrm{St} = \frac{2}{9}\frac{\rho_p}{\rho}\frac{\dot{\gamma}_0 a^2}{\nu}$.

While being moved with the flow, the solid spheres undergo hard-sphere collisions for which the two-coefficient model due to Yamamoto *et al.*[17] was adopted. The two coefficients are the restitution coefficient e and the friction coefficient μ. In a collision, two spheres i and j having pre-collision linear and angular velocity $\mathbf{u_{pi}}$, $\mathbf{u_{pj}}$, $\boldsymbol{\omega_{pi}}$, and $\boldsymbol{\omega_{pj}}$ exchange momentum according to

$$\tilde{\mathbf{u}}_{\mathbf{pi}} = \mathbf{u_{pi}} + \mathbf{J}, \quad \tilde{\mathbf{u}}_{\mathbf{pj}} = \mathbf{u_{pj}} - \mathbf{J}, \quad \tilde{\boldsymbol{\omega}}_{\mathbf{pi}} = \boldsymbol{\omega_{pi}} + \frac{5}{2a}\mathbf{n} \times \mathbf{J},$$
$$\tilde{\boldsymbol{\omega}}_{\mathbf{pj}} = \boldsymbol{\omega_{pj}} + \frac{5}{2a}\mathbf{n} \times \mathbf{J}. \tag{1}$$

The superscript $\sim$ indicates post-collision quantities and $\mathbf{n}$ is the unit vector pointing from the center of sphere i to the center of sphere j. The momentum exchange vector $\mathbf{J}$ can be decomposed in a normal and tangential part: $\mathbf{J} = J_n\mathbf{n} + J_t\mathbf{t}$. The tangential unit vector $\mathbf{t}$ is in the direction of the pre-collision slip velocity $\mathbf{c_c}$ between the sphere surfaces at the point of contact,

$$\mathbf{c_c} = (\mathbf{u_{pj}} - \mathbf{u_{pi}}) - [(\mathbf{u_{pj}} - \mathbf{u_{pi}}) \cdot \mathbf{n}]\mathbf{n} - a\boldsymbol{\omega_{pi}} \times \mathbf{n} - a\boldsymbol{\omega_{pj}} \times \mathbf{n}. \tag{2}$$

In the collision model the components of the momentum exchange vector are

$$J_n = \frac{(1+e)}{2}(\mathbf{u_{pj}} - \mathbf{u_{pi}}) \cdot \mathbf{n}$$
$$J_t = \min\left[-\mu J_n, \frac{1}{7}|\mathbf{c_c}|\right]. \tag{3}$$

As indicated in the expression for J_t, the collision switches between a slipping and a sticking collision at $-\mu J_n = \frac{1}{7}|\mathbf{c_c}|$. In some simulations the friction coefficient μ was set to infinity which means that in such a simulation a collision always is a sticking collision (with $J_t = \frac{1}{7}|\mathbf{c_c}|$). If one of the two spheres (say sphere j) in a collision is a fixed sphere attached to the bottom wall, the update equations for sphere i are $\tilde{\mathbf{u}}_{\mathbf{pi}} = \mathbf{u_{pi}} + 2\mathbf{J}$, $\tilde{\boldsymbol{\omega}}_{\mathbf{pi}} = \boldsymbol{\omega_{pi}} + \frac{5}{a}\mathbf{n} \times \mathbf{J}$; and the same expression for $\mathbf{J}$ (Eq. (3)) applies.

We restrict ourselves to binary collisions between spheres and do not consider enduring contacts between spheres. Given the denseness of the suspension this implies continuous (though very often minute) motion of spheres deeper in the bed. It also implies that deeper in the bed collisions between spheres are particularly frequent and at the same time very weak. Our event-driven collision algorithm can efficiently deal with this; we keep track of each individual collision, no matter how closely spaced in time, and do not allow (and do not have) overlap of spheres.

The flow systems are periodic in the x (streamwise) and y (lateral) direction. At every solid surface (bounding upper and lower wall, as well as the sphere surfaces) no-slip applies for the liquid. Moving spheres do not collide with the bounding walls so that particle-wall collision parameters are not relevant. The bottom wall is shielded by a dense layer of immobile spheres directly attached to it; the mobile spheres also do not collide with the upper wall since Shields and Reynolds numbers are small to moderate so that spheres do not move far in vertical direction; if spheres move they stay closely above the granular bed.

In terms of physical (as opposed to computational) dimensionless numbers, the parameter space is thus five-dimensional: θ, Re, $\frac{\rho_p}{\rho}$, e, and μ. One of our primary interests is in how erosion and solids mobility depend on the Shields number θ under laminar flow conditions, and if we can identify a critical Shields number θ_c below which the solids are (virtually) immobile. For this reason in this study Shields numbers in the range 0.05 to 0.8 have been investigated since experiments[1,5] indicate θ_c to be well within this range, at least for laminar flow. Particle-based Reynolds numbers have been varied in the range of 0.02 to 0.6. We anticipate the role of the density ratio (other than via θ) to be minor given the limited influence of inertia: the flow is laminar and the spheres move slowly ($\mathrm{St} \leq 2$). As the default density ratio we took $\frac{\rho_p}{\rho} = 4.0$, a value of 3.0 was considered as well, mainly to compare situations that have the same Shields and Reynolds number but a different density ratio so that the hypothesis that inertia is of limited importance can be assessed.

In liquid-solid systems the role of the restitution coefficient is relatively weak (much weaker than in gas-solid systems) because energy dissipation mainly occurs in the liquid phase,[18] not so much as a result of solid-solid contact. We set $e = 1.0$ in all our flow simulations. Frictional (i.e., non-smooth) collisions transfer—next to linear momentum—angular momentum between particles, which in a solid bed mobilized by a shear flow is a relevant mechanism: The shear flow exerts a torque on the upper spheres; and we expect that collisional friction influences the rotational

behavior of the spheres deeper in the bed and thus the behavior of the bed as a whole. To investigate this we compare simulations involving frictionless collisions (smooth particles, $\mu = 0$) with simulations that have $\mu = 0.1$ (which was our base-case friction coefficient) and up to $\mu \to \infty$ (sticky collisions).

In addition to a physical parameter space, we deal with numerical settings, the influence of which needs to be considered. These settings are discussed at the end of Sec. III that describes the numerical method.

III. MODELING APPROACH

As in many of earlier works on direct simulations of liquid-solid suspensions with full resolution of the interfaces, we used the lattice-Boltzmann (LB) method[11,12] to solve for the flow of the interstitial liquid. The method has a uniform, cubic grid (grid spacing Δ) on which fictitious fluid particles move in a specific set of directions and collide to mimic the behavior of an incompressible, viscous fluid. The specific LB scheme employed here is due to Somers;[19] also see Eggels and Somers.[20] The no-slip condition at the spheres' surfaces was dealt with by means of an immersed boundary (or forcing) method.[13,14] In this method, the sphere surface is defined as a set of closely spaced points (the typical spacing between points is 0.7Δ), not coinciding with lattice points. At these points the (interpolated) fluid velocity is forced to the local velocity of the solid surface according to a control algorithm; the local solid surface velocity has a translational and rotational contribution. Adding up (discrete integration) of the forces needed to maintain no-slip provides us with the (opposite; action equals minus reaction) force the fluid exerts on the spherical particle. Similarly the hydrodynamic torque exerted on the particles can be determined. Forces and torques are then used to update the linear and rotational equations of motion of each spherical particle.

We have validated and subsequently used this method extensively to study the interaction of (static as well as moving) solid particles and Newtonian and non-Newtonian fluids. For instance, simulation results of a single sphere sedimenting in a closed container were compared with particle image velocimetry (PIV) experiments of the same system and showed good agreement in terms of the sphere's trajectory, as well as the flow field induced by the motion of the falling sphere up to $\mathrm{Re} \approx 30$.[21] For dense suspensions (with volume-averaged solids volume fractions up to 0.53), Derksen and Sundaresan[18] were able to quantitatively correctly represent the onset and propagation of instabilities (planar waves and two-dimensional voids) of liquid-solid fluidization as experimentally observed.[22,23]

It should be noted that having a spherical particle on a cubic grid requires a calibration step, as earlier realized by Ladd.[24] He introduced the concept of a hydrodynamic radius. The calibration involves placing a sphere with a given radius a_g in a fully periodic cubic domain in creeping flow and (computationally) measuring its drag force. The hydrodynamic radius a of that sphere is the radius for which the measured drag force corresponds to the expression for the drag force on a simple cubic array of spheres due to Sangani and Acrivos[25] which is a modification of the analytical expression due to Hasimoto.[26] Usually a is slightly bigger than a_g with $a - a_g$ typically equal to half a lattice spacing or less.

In previous papers,[10,18,21,27,28] we have repeatedly checked the impact of spatial resolution on the results of our simulations and we consistently concluded that a resolution such that a corresponds to 6 lattice spacings is sufficient for accurate results (based on comparison with higher resolution simulations and with experimental data) as long as particle-based Reynolds numbers do not exceed values of the order of 30. The simulations presented in this paper all have a resolution such that $a = 6\Delta$. Once the spatial resolution is fixed, the temporal resolution of the LB simulations goes via the choice of the kinematic viscosity. In all simulations the viscous time scale $\frac{a^2}{\nu}$ corresponds to 360 time steps (i.e., $\nu = 0.1$ in lattice units).

The time-step driven LB updates are linked with an event-driven algorithm for the hard-sphere collisions. Once a collision is being detected, all particles are frozen and the collision is carried out which implies an update of the linear velocities (and also angular velocities if $\mu \neq 0$) of the two spheres involved in the collision event. Subsequently all spheres continue moving until the end of the LB time step, or until the next collision.

The fixed-grid simulations involving dense suspensions as discussed here require explicit inclusion of sub-grid lubrication forces.[29] The low-Reynolds number expression for the radial lubrication force on two equally sized solid spheres i and j having relative velocity $\Delta\mathbf{u_{ij}} \equiv \mathbf{u_{pj}} - \mathbf{u_{pi}}$ reads[16]

$$F_{lub} = \frac{3}{2}\pi\rho\nu a^2 \frac{1}{s}\left(\mathbf{n}\cdot\Delta\mathbf{u_{ij}}\right), \quad \mathbf{F_{lub,j}} = -F_{lub}\mathbf{n},$$
$$\mathbf{F_{lub,i}} = F_{lub}\mathbf{n}, \tag{4}$$

with s the smallest distance between the sphere surfaces $s \equiv \left|\mathbf{x_{pj}} - \mathbf{x_{pi}}\right| - 2a$, and (as explained earlier in the context of collision modeling) $\mathbf{n}$ the unit vector pointing from the center of sphere i to the center of sphere j. Tangential lubrication forces and torques have not been considered since they are much weaker than the radial lubrication force; the former scale with $\ln\left(\frac{a}{s}\right)$, the latter with $\frac{a}{s}$. The expressions in Eq. (4) need to be tailored for use in lattice-Boltzmann simulations:[18,29] (1) The lubrication force needs to be switched off when sphere surfaces are sufficiently separated in which case the LBM can accurately account for the hydrodynamic interaction between the spheres (typically if $s > \Delta$). (2) The lubrication force needs to saturate when solid surfaces are very close to account for surface roughness and to avoid very high levels of the lubrication force that could lead to unphysical instabilities in the simulations.

A smooth way to turn on and off the lubrication force has been proposed by Nguyen and Ladd;[29] instead of Eq. (4) one writes

$$F_{lub} = \frac{3}{2}\pi\rho\nu a^2\left(\frac{1}{s} - \frac{1}{\delta}\right)\left(\mathbf{n}\cdot\Delta\mathbf{u_{ij}}\right) \quad \text{if} \quad s \leq \delta, \quad \text{and}$$
$$F_{lub} = 0 \quad \text{if } s > \delta, \tag{5}$$

with the modeling parameter δ as the distance between solid surfaces below which the lubrication force becomes active.

A second modeling parameter (ε) is the distance below which the lubrication force gets saturated: $F_{lub} = \frac{3}{2}\pi\rho\nu a^2 \left(\frac{1}{\varepsilon} - \frac{1}{\delta}\right)\left(\mathbf{n}\cdot\Delta\mathbf{u_{ij}}\right)$ if $s \le \varepsilon$. The default settings for the lubrication force modeling parameters were $\delta = 0.2a$ and $\varepsilon = 2\cdot 10^{-4}a$.

To summarize the numerical settings: the uniform grid spacing was $\Delta = \frac{a}{6}$; the time step was $\Delta t = \frac{a^2}{360\nu}$; the default numerical settings for the of the lubrication force were $\delta = 0.2a$ and $\varepsilon = 2\cdot 10^{-4}a$. The sensitivity with respect to the latter settings has been investigated.

In addition to physical and numerical parameters, the necessarily finite size of the flow domain adds to the dimensionality of the parameter space. The default aspect ratios were $\frac{L}{a} = 20$, $\frac{W}{a} = 10$ and $\frac{H}{a} = 20$. The particle bed typically occupies the lower half of the flow domain so that the open space above the bed has a height of approximately $10a$. With these default settings the number of spheres in a simulation amounts to 286, of which 242 are mobile, and 44 make up the monolayer glued to the bottom plate. We investigated the impact of the aspect ratios, as well as the impact of the depth of the particle bed on its global behavior. In an earlier paper on shear flow above beds of fixed spherical particles[10] it was shown that the influence of the height of the free space above the bed on drag and lift forces could be largely eliminated if we scale the relevant flow quantities (velocities, hydrodynamic forces and torques) by means of the shear rate resulting from the slope of the linear velocity profile well above the bed: $\dot\gamma_0 = \frac{d\langle u_x\rangle}{dz}$.

IV. RESULTS

A. Impressions of liquid flow and particle motion

We first consider three reference simulations that have the default numerical settings and default aspect ratios as defined above. They also have the same density ratio $\frac{\rho_p}{\rho} = 4.0$, collision parameters ($e = 1.0$ and $\mu = 0.1$), and approximately the same Reynolds number. They differ with respect to their Shields number. The steady-state, time and space (x and y) averaged interstitial liquid velocity profiles are plotted in Figure 2. From these profiles $\dot\gamma_0$ is derived for each simulation and subsequently Re and θ are determined. The three cases have $\mathrm{Re} = 0.121$, $\theta = 0.101$ (case A); $\mathrm{Re} = 0.122$, $\theta = 0.204$ (case B); $\mathrm{Re} = 0.126$, $\theta = 0.420$ (case C). Figure 2 also shows the solids volume fraction profiles at a resolution finer than the particle radius. The coherent fluctuations in ϕ are the consequence of the discrete nature of the solids phase consisting of uniformly sized spheres, and the fact that the relatively shallow layer of spheres was built up starting from spheres glued to the flat bottom plate. The partial entrainment of solid particles by the shear flow at the top of the solids bed can be witnessed from the solids volume fraction profiles extending higher up for higher Shields numbers. The latter is further detailed in single realizations of the particle positions in the bed in Figure 3, with the particles colored according to their absolute velocity; and in Figure 4 that shows vertical and streamwise velocities of individual particles as a function of their vertical (z) center location in the bed (this way of representing the data was inspired by Figure 2 in Mouilleron *et al.*[4]). The higher the Shields numbers, the more particles attain higher velocities, and the liquid flow is able to mobilize particles deeper in the bed.

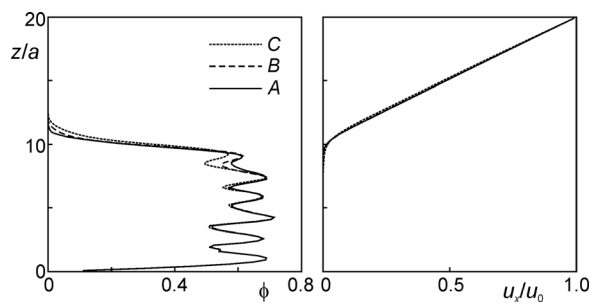

FIG. 2. Average solids volume fraction (left) and interstitial streamwise liquid velocity (right) as a function of the vertical coordinate z for the three reference cases A, B, and C as identified in the text.

Charru *et al.*[1] observed in their experiments a slow compaction of the granular bed as a result of rearrangement of particles due to the motion brought about by the sheared liquid above the bed; a process that took place on a timescale of the order of $\frac{10^6}{\dot\gamma_0}$. This timescale is well beyond our computational capabilities; the simulations reported here typically run until $t \approx \frac{3\cdot 10^2}{\dot\gamma_0}$ starting from $t = 0$ when we start moving the upper wall over a zero-velocity liquid and particle field. It then takes approximately $30\frac{a^2}{\nu}$ ($\approx \frac{4}{\dot\gamma_0}$ with the default computational settings) for the liquid momentum to penetrate down to the granular bed. Impressions of the time evolution of the reference simulations are given in Figure 5, where it should be noted that all three reference simulations started from the same sphere configuration. The bed height (defined as the average z-center position of the top 44 spheres in the bed) and the average translational kinetic energy per sphere are used in Figure 5 as global characteristics of the beds. For the lowest Shields number (case A) a compaction of the bed and very little kinetic energy are observed. For this case A bed height and kinetic energy are in fact time-correlated: peaks in kinetic energy are associated with small humps in bed height and occur when a sphere hops over another sphere and falls back in the bed. Also for the intermediate Shields number (case B) the bed compacts a little over time. Compaction, however, competes with entrainment of particles by the shear flow in this case. The kinetic energy hardly ever getting zero in case B implies (almost) continuous motion of spheres. For the higher Shields number (case C) particle entrainment by the flow almost from the start compensates compaction so that initially the bed height increases and then

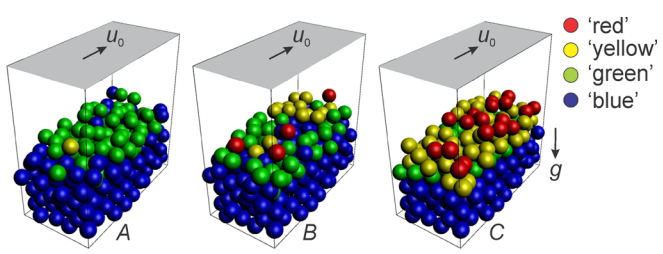

FIG. 3. (Color online) Single realizations of the reference sheared granular beds A, B, and C. The spheres are shaded/colored according to their absolute velocity: red: $|\mathbf{u_p}| \ge 0.1\dot\gamma_0 a$; yellow: $0.1\dot\gamma_0 a > |\mathbf{u_p}| \ge 0.01\dot\gamma_0 a$; green: $0.01\dot\gamma_0 a > |\mathbf{u_p}| \ge 0.001\dot\gamma_0 a$; blue: $0.001\dot\gamma_0 a > |\mathbf{u_p}|$.

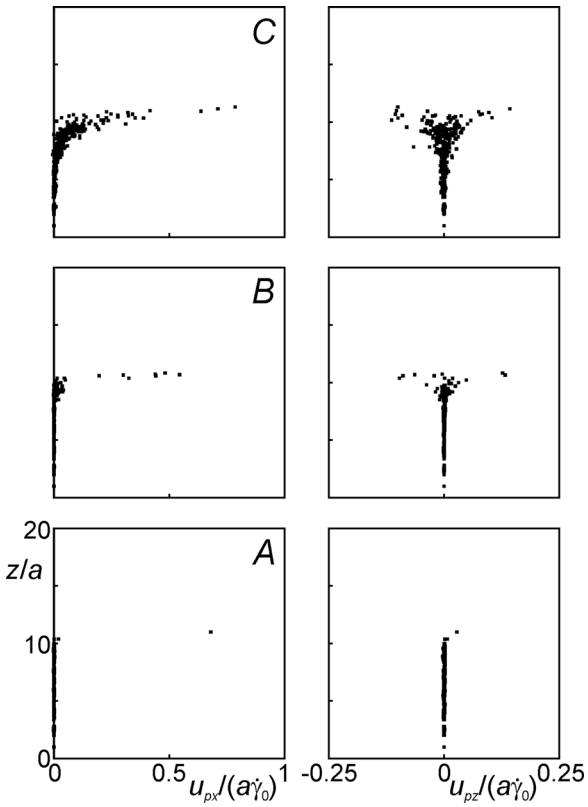

FIG. 4. Individual particle velocities (left: x-component; right: z-component) as a function of the z-location of the particle. Three independent realizations ($3 \times n_p$ data points per panel, with $n_p = 286$ the number of spheres in each simulation). From bottom to top simulations A, B, and C.

reaches a quasi steady state after approximately $t \approx \frac{160}{\dot{\gamma}_0}$. The particle bed is in continuous motion for this case, i.e., the average particle kinetic energy never drops to zero.

B. Impact of computational and modeling choices

In this section, the impact of the modeling choices on the overall behavior of the granular beds is assessed. In addition to characterizing the beds in terms of their height and translational solids kinetic energy, other global measures will be used for comparison, such as the solids volumetric flux.

The finite number of spheres in the default cases (286 of which 242 are mobile and 44 glued to the bottom plate) makes the results sensitive to the initial bed configuration as can be seen in Figure 6. Here, the intermediate Shields number case B is repeated starting from a sphere assembly created with random numbers independent of the numbers that created the original bed. The alternative bed (case $B2$) starts as slightly thicker (by $0.1a$) compared to the original bed. The $B2$-bed evolves to a height comparable to the eventual height of case B, and does so on a similar time scale. The kinetic energy fluctuations (Figure 6, bottom panel) of the two cases are similar as well. Quantitatively there are differences. The time-averaged values of the kinetic energy signals shown in Figure 6 differ by some 15%, and the RMS values of the fluctuations by 1% (the actual numbers are given in the figure caption); this is indicative for the uncertainty as a result of the finite number of spheres per simulation and the

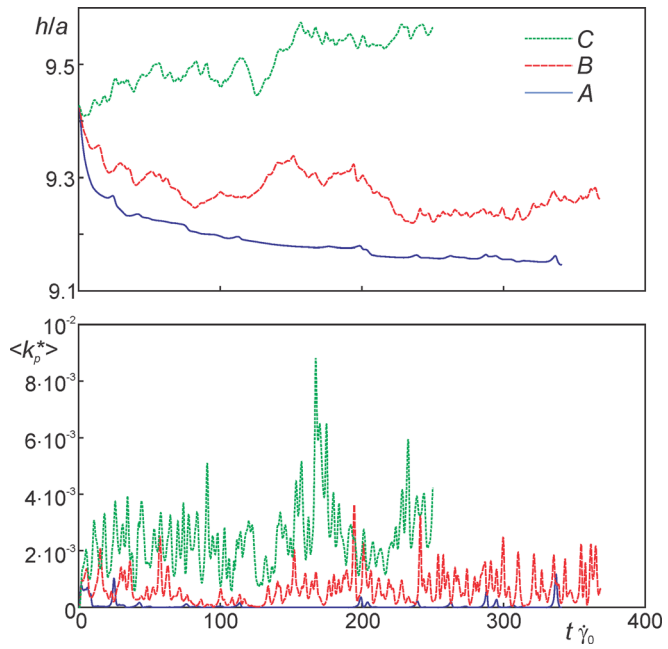

FIG. 5. (Color online) Time series of bed height (top) and average kinetic energy of the solid particles (bottom). The bed height is defined as the average z-center-position of the 44 particles highest up in the bed. The particle's linear kinetic energy is non-dimensionalized according to $k_p^* \equiv \frac{\frac{1}{2}|\mathbf{u_p}|^2}{(\dot{\gamma}_0 a)^2}$; $\langle k_p^* \rangle$ indicates averaging over all particles in the bed. Cases A, B, and C as indicated.

finite system size and should be kept in mind when interpreting the results to come.

With our simulations we intend to mimic deep granular beds, i.e., beds that extend deeper than the liquid flow is able to penetrate. To check if this is the case we again took simulation B and compared it to a case where we had one extra

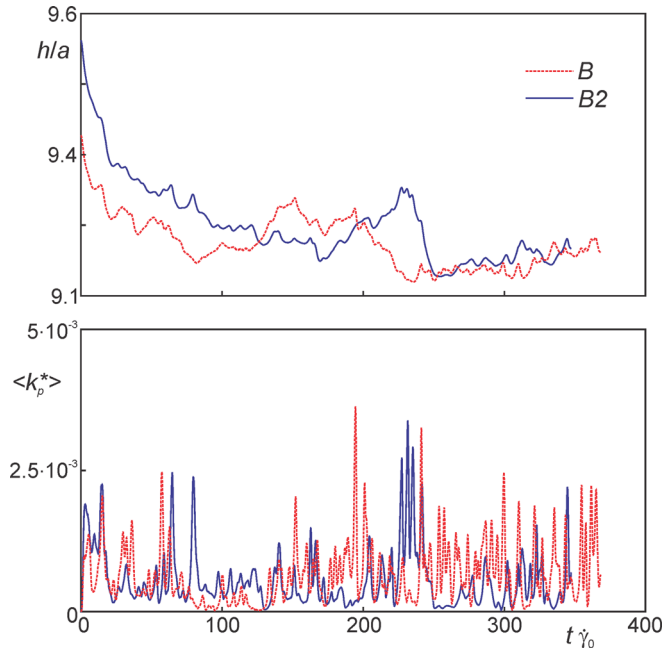

FIG. 6. (Color online) Time series of bed height (top) and average kinetic energy of the solid particles (bottom). Comparison between two cases with the same settings but different initial particle configuration. The time-averaged kinetic energy for case B is $6.48\cdot10^{-4}$, for case $B2$ it is $5.52\cdot10^{-4}$; standard deviations are $5.19\cdot10^{-4}$ and $5.13\cdot10^{-4}$ for B and $B2$, respectively.

layer of spheres (case B^+) and a case with one less layer of spheres (case B^-). The three beds were created independently so that (also) configuration effects as discussed above are anticipated. When adding or removing a sphere layer, the liquid layer above the bed was kept at approximately the same thickness. Given the unpredictability in the way the particles organize themselves and get entrained as a result of the flow the shear rates and thus Re and θ differ slightly between case B: $\mathrm{Re}=0.122$, $\theta=0.204$; B^+: $\mathrm{Re}=0.118$, $\theta=0.197$; and B^-: $\mathrm{Re}=0.131$, $\theta=0.218$. In Figure 7 the cases are compared in terms of time series of translational kinetic energy. Since now the number of spheres per simulation is different we present the non-dimensional total kinetic energy contained in translational motion of all spheres involved in each simulation ($n_p\langle k_p^*\rangle$ with n_p the number of spheres per simulation). For sufficiently deep granular beds, this quantity should become independent of the depth of the bed.

Results in Figure 7, however, indicate a systematic effect of bed height: They show that the shallowest bed has on average significantly higher kinetic energy levels compared to the other two beds that have approximately the same average kinetic energy. The kinetic energy fluctuation levels are roughly the same for the three cases. To further investigate the difference in kinetic energy between case B^- on one side and B and B^+ on the other side, the cases are further compared in terms of average z-profiles of solids volume fraction φ, streamwise liquid velocity u_x, and particle volume flux ϕu_{px} in Figure 8 (we present particle flux rather than particle velocity u_{px} to emphasize volumetric transport of solids; not only the solids velocity matters, also how many particles have that velocity).

When here and later in this paper average data in terms of z-profiles are presented averaging is done in space over the homogeneous x and y-direction and over a time span starting at $t=\frac{100}{\dot\gamma}$ until (at least) $t=\frac{200}{\dot\gamma}$. In this time interval the flow systems are largely in a stationary state (see, e.g., Figure 5) except for a slight compaction of the bed if θ is small (typically $\theta<0.2$).

In Figure 8 the most significant difference between the cases is the much greater particle flux in case B^-, which explains its greater kinetic energy. Integrating the $\phi u_{px}$with respect to z gives the total solids volumetric flow rates per unit (y) width as $0.0348\dot\gamma_0 a^2$ for case B^+, $0.0326\dot\gamma_0 a^2$ for case

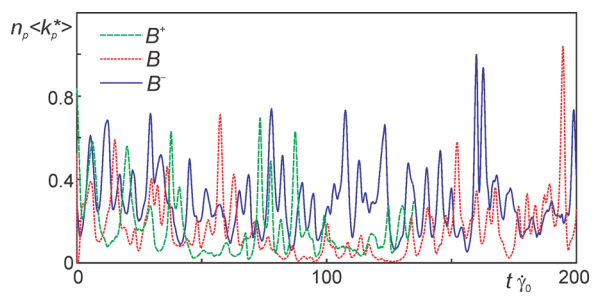

FIG. 7. (Color online) Time series of the total kinetic energy of the solid particles. Comparison between different granular bed heights. The time-averaged total kinetic energy for case B^-, B, and B^+ are 0.290, 0.185, and 0.168, respectively. The root-mean-square values of the fluctuations are 0.148, 0.148, and 0.158 for cases B^-, B, and B^+, respectively.

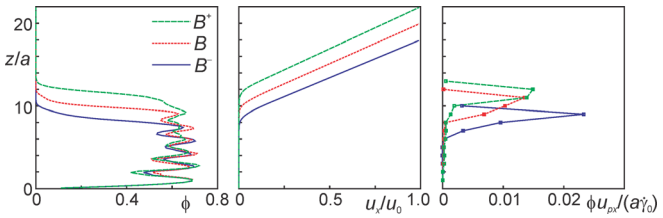

FIG. 8. (Color online) Average solids volume fraction (left), streamwise liquid velocity (middle), and solids flux (right) as a function of z. Comparison between different granular bed heights. Variants of case B ($\mathrm{Re}\approx 0.12$, $\theta\approx 0.20$).

B, and $0.0395\dot\gamma_0 a^2$ for case B^-, with $\dot\gamma_0$ approximately equal in the three cases (see the middle panel of Figure 8). Given the shape of the ϕu_{px}-profiles, these differences are not a result of particle motion near the bottom of the shallow bed. The primary reason is the shallow bed being rougher at the surface so that the shear flow is better able to penetrate the bed and move the spheres. We quantify bed roughness by determining the root-mean-square of the z-center locations of the top 44 spheres: $\frac{z_{rms}}{a}=\frac{1}{a}\sqrt{\sum_{i=1}^{n}\left[\frac{z_{c,i}^2}{n}-\left(\frac{z_{c,i}}{n}\right)^2\right]}$ (with $n=44$). Time average values (obtained after steady state was reached) are $\overline{\frac{z_{rms}}{a}}=0.57$, 0.47, and 0.49 for B^-, B, and B^+. respectively. The higher surface roughness for bed B^- is due to fewer sphere layers above the flat wall and thus less packing opportunity for spheres. This makes shallower beds have rougher bed surfaces. The fairly good correspondence between beds B and B^+ in terms of solids flux and bed roughness indicates that the depth of granular bed B (ten times the sphere radius a) is sufficient to have limited influence on its overall dynamics; $10a$ is the default depth we work with in the rest of this paper.

The subgrid lubrication force is one of the main modeling steps in the simulations. To assess the influence of lubrication forces on the overall granular bed dynamics we compare the results of three simulations: Case C which has $\theta=0.420$ and for the rest default settings; a case as Case C but without lubrication: Case C_{nlub}; and a case as Case C where the saturation distance ε of the lubrication force was increased by a factor 10: instead of the default $\varepsilon=2\cdot10^{-4}a$ it was set to $\varepsilon=2\cdot10^{-3}a$. The latter case is referred to as C_{rlub}. All three cases start with the same sphere configuration.

The results in Figure 9 show that the lubrication force plays a large role in the amount of solids being transported. The effect of its precise settings, however, is less significant. Clearly the mobility of the bed increases without lubrication force (see the right panel of Figure 9). This is because it is now easier for spheres to separate and move over the bed surface (separating spheres induce an attractive lubrication force). In the same spirit, lubrication makes it harder for spheres that are detached from the bed to settle back into it due to its repulsive nature for approaching particles.

The friction coefficient in particle-particle collisions is an unknown factor. For instance, in the detailed experimental work due to Charru and co-workers[1,2,4] no data for the friction coefficient is provided (the papers do consider "effective" friction coefficients but these are overall ratios of shear and

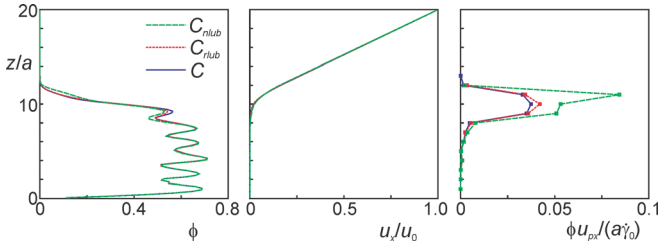

FIG. 9. (Color online) Average solids volume fraction (left), streamwise liquid velocity (middle) and solids flux (right) as a function of z. Comparison between different settings for the lubrication force: C has standard settings, C_{rlub} has a 10 times smaller lubrication force saturation level ($\varepsilon = 2 \cdot 10^{-3} a$), C_{nlub} has no lubrication force. Case C: Re ≈ 0.12, $\theta \approx 0.42$.

normal particle stress in the context of e.g., Bagnold's model,[30] not the "microscopic" friction coefficient μ). It is anticipated, however, that the level of microscopic friction between particles is a relevant parameter for bed mobility, with a-priori unknown consequences. Increased friction makes particles stick more, at least in terms of their relative tangential motion thus possibly making it harder to mobilize the bed. On the other side, more friction could facilitate a sphere to roll over a neighboring sphere at the bed surface. As we did for assessing the effect of lubrication, we took case C ($\theta = 0.420$) as a base case and ran cases that had friction coefficients μ different from its base-case value of 0.1. Statistical data were collected in the same manner as indicated above. In addition to solids volume fraction and solids flux, also data regarding the spheres' angular velocity component along the y-axis (which is the main axis of rotation given the overall $\frac{\partial u_x}{\partial z}$ fluid velocity gradient) are discussed since frictional collisions transfer tangential momentum.

The behavior of the bed clearly depends on the friction coefficient, see Figure 10. Higher friction increases the particle flux in the very top layer; less friction allows for more motion (translation and rotation) deeper in the bed. The easier rolling of top spheres over underlying ones at higher friction is responsible for the former effect. The deeper penetration of motion in the bed in the absence of friction is induced by the shear flow that makes the spheres in the top layer strongly spin. This spinning is transferred deeper in the bed by the interstitial fluid and not hindered by (dry) friction. Only a little friction ($\mu = 0.1$) inhibits this process. The rotation of spheres inside the bed enhances the spheres' mobility (also translational) deeper in the bed. A different representation of largely the same data but now in terms of average solids and liquid velocities shows minor sensitivity with respect to μ (Figure 11). This representation does show that (at least for $\theta \approx 0.4$) the solids velocity slightly lags the liquid velocity which agrees with experimental observation in Mouilleron *et al.*[4]

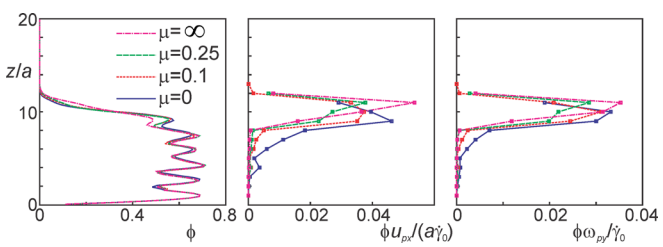

FIG. 10. (Color online) Average solids volume fraction (left), solids flux (middle), and particle y-angular velocity weighted with the solids volume fraction (right) as a function of z. Comparison between different settings of friction coefficient μ. Variants of case C. Case C: Re ≈ 0.12, $\theta \approx 0.42$.

In their experiments, Charru *et al.*[1] evaluated the probability density function (PDF) of the streamwise component of particle velocity. They observed exponential PDFs that—if particle velocity was scaled with $\dot{\gamma}a$—were independent of θ (as long as $\theta \leq 0.24$). The latter result is not to be expected from our simulations: e.g., in Figure 5 the kinetic energy of particles scaled with $(\dot{\gamma}a)^2$ clearly depends on θ. It has to be realized, however, that in the experiments the Shields number was varied by changing the shear rate $\dot{\gamma}$ while keeping the other parameters in θ constant. In the simulations, gravitational acceleration g was varied to vary the Shields number while $\dot{\gamma}$ was (mostly) kept constant (we used this strategy to allow for changing θ while keeping Re constant). This implies that scaling particle velocity PDFs with the Stokes settling velocity $U_s = \frac{2}{9}\frac{g(\rho_p - \rho)a^2}{\rho\nu}$ in the simulations is equivalent to scaling with $\dot{\gamma}a$ in the experiments; note that the Shields number is proportional to the ratio $\frac{\dot{\gamma}a}{U_s}$. Such PDF scaling of the simulations should give θ-independent results to be consistent with the experimental results.

Figure 12 shows particle velocity PDFs derived from simulations with $\theta = 0.15$, 0.20, and 0.40 (all at Re $\approx$0.12). As in the experiments[1] a cut-off velocity U_{co} was used to discard particles that hardly move. The cut-off in the experiments was $\frac{U_{co}}{U_s} = 0.02$ and the same value was adopted in the simulations. Similar and more or less exponential velocity PDF's can be observed in Figure 12 for the three Shields numbers. For $\theta = 0.15$ experimental data and simulated data can be directly compared; the average streamwise particle velocities are $0.32U_s$ and $0.31U_s$ in experiment and simulation, respectively. Different from the experiments, however, the average particle velocity does appreciably depend on the choice of the cut-off velocity: if $\frac{U_{co}}{U_s}$ is reduced by a factor of

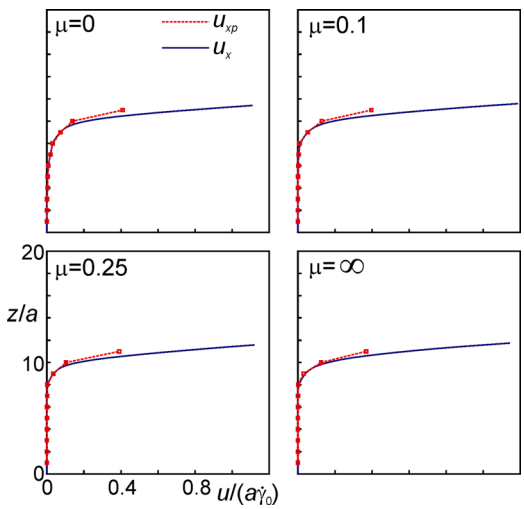

FIG. 11. (Color online) Average solids and liquid velocity for four variants of case C (Re ≈ 0.12, $\theta \approx 0.42$), which only differ by the friction factor μ. The solids velocity is indicated only if locally $\phi > 0.025$.

two, the average velocity goes down by some 20%. This implies that in the simulations there is a less clear distinction between moving and static spheres compared to the experiments.

C. Shields and Reynolds number effects

We now fix the friction coefficient to $\mu = 0.1$ and investigate how the bed mobility depends on the Shields number, the Reynolds number, and the solid-over-liquid density ratio. Based on the results (mainly experimental) from the literature it is anticipated that the Shields number is the primary parameter for the onset of bed mobility and we want to see if a critical Shields number can be identified based on the results of our simulations.

The velocity profiles in Figure 13 show a clear trend of increasing solids velocity if the Shields number is increased. As argued above, a more sensitive parameter for bed mobility is the solids volumetric flow rate that combines particle velocity and (local) solids volume fraction. Integral volumetric solids fluxes (symbol φ', solids volume per unit time and unit lateral (y) width) as a function of θ are given in Figure 14. Next to sensitivities with respect to the Shields number, the figure considers effects of Re (top panel) and $\frac{\rho_p}{\rho}$ (bottom panel). If we would want to identify a critical Shields number in the data set displayed in Figure 14, it would be between the second and third data point, i.e., $0.10 < \theta_c < 0.15$. Between $\theta = 0.10$ and $\theta = 0.15$ a fairly clear transition takes place from a virtually immobile bed to a bed with a somewhat significant solids flux. More interestingly, the transition takes place in the same θ-interval irrespective of the Reynolds number and the density ratio (within the parameter range investigated of course).

The θ_c interval as identified through the simulations is well in line with Ouriemi *et al.*'s experimental observations[5] that indicate $\theta_c = 0.12 \pm 0.03$ for $4 \cdot 10^{-6} < \mathrm{Re} < 0.2$ (note that Ouriemi *et al.* based their Reynolds number definition on sphere diameter, not on sphere radius). In turn, the results due

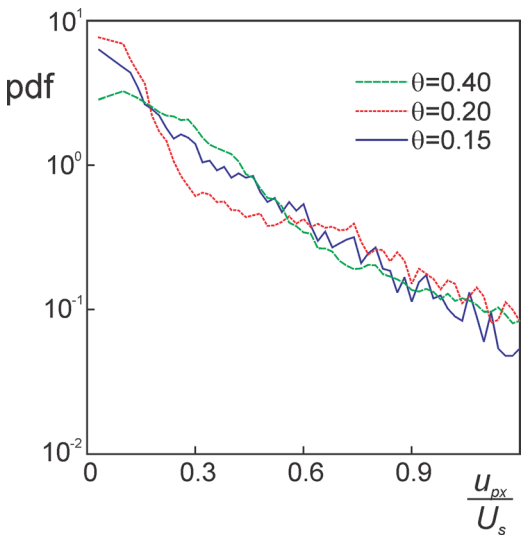

FIG. 12. (Color online) PDFs of streamwise particle velocity for three values of the Shields number as indicated. Re ≈ 0.12. Particles with streamwise velocity less than $U_{co} = 0.02U_s$ have been discarded in the PDFs.

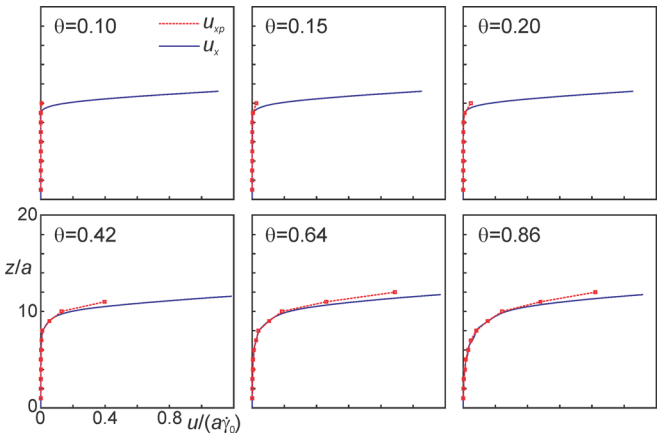

FIG. 13. (Color online) Average solids and liquid velocity for four variants for different Shields numbers and further base-case conditions. The solids velocity is indicated only if locally the solids volume fraction exceeds 2.5% ($\phi > 0.025$).

to Ouriemi *et al.* were compared with a large body of experimental data collected from the literature; see Figure 5 in Ouriemi *et al.*[5] These older data only partly agree with Ouriemi *et al.*'s results. Different from Ouriemi *et al.*, the trend in some of the older data with respect to the Reynolds number is a fairly significant increase in θ_c if Re decreases in ranges where Ouriemi *et al.* have constant θ_c. Typically θ_c would increase from 0.1 for $\mathrm{Re} = 0.025$ to 0.2 for $\mathrm{Re} = 3 \cdot 10^{-4}$ (e.g.,

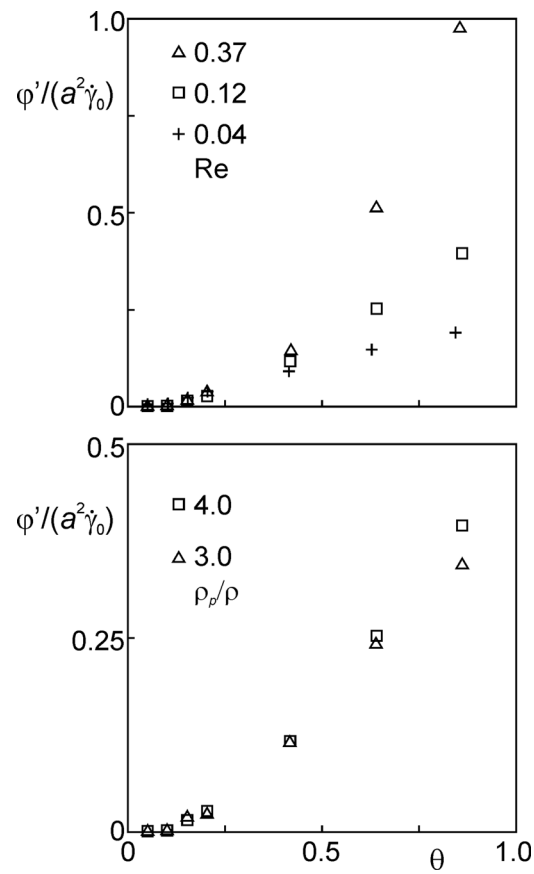

FIG. 14. Averaged volumetric flux per unit lateral width of solids ϕ' as a function of the Shields number θ. Top: for $\frac{\rho_p}{\rho} = 4.0$ and various Re; bottom: for $\mathrm{Re} = 0.12$ and $\frac{\rho_p}{\rho} = 4.0$ and 3.0. Note the different vertical scales in the two panels.

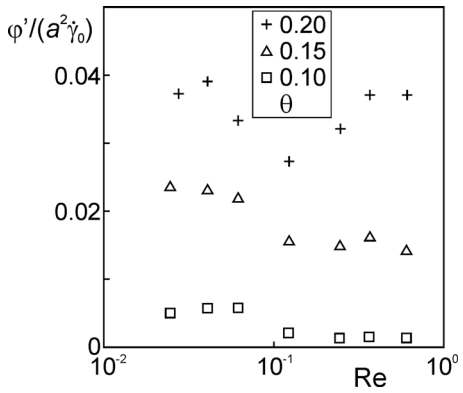

FIG. 15. Average volumetric flux per unit lateral width of solids ϕ' as a function of Re for three (small) values of θ.

the data from White[31]). To check if we could discern a trend with Re, we did a few additional simulations around the suspected θ_c for various Reynolds numbers, see Figure 15. As before, we used the solids volume flux per unit (lateral) width as a metric for bed mobilization. There is no clear trend with Re in Figure 15. There might be a weak trend towards lower solid fluxes for higher Reynolds numbers. If anything, such a trend would imply a very weak decrease in critical Shields number with decreasing Re, opposite to the trend in the data as compiled by Ouriemi *et al.*[5]

Away from the critical Shields number, Reynolds number effects on bed mobility are very significant (see the upper panel of Figure 14). For instance, at $\theta = 0.8$ the solids volume flux increases by a factor of 5 if Re goes from 0.04 to 0.37. The density ratio is a less critical parameter: Changing the density ratio has minor effect on bed mobility as a function of θ (see the lower panel of Figure 14).

D. Inside the sheared granular bed

For a mechanistic view of solid bed erosion we now briefly look into forces on individual spheres in the granular bed. In Figure 16 cross sections through beds sheared at different Shields numbers are shown. The liquid phase is colored with pressure contours. The vectors indicate the resolved hydrodynamic force (i.e., not the sub-lattice lubrication force) and velocity of individual spheres in the bed. Clearly the spheres high up in the bed feel strong differential pressure and associated hydrodynamic forces. For the higher Shields numbers, pressure fluctuations extend deeper in the bed. Non-dimensional forces and velocities increase with increasing Shields number. Hydrodynamic force and velocity are not aligned which is obvious given the obstruction formed by surrounding particles, and gravity and lubrication also acting on the particles.

To relate to the earlier observations regarding bed mobility as a function of the Shields number and the notion of a critical Shields number in the range $0.10 < \theta_c < 0.15$ force distribution functions are analyzed. The vertical component of the hydrodynamic force is relevant since it would be responsible for overcoming net gravity, lifting a sphere up so that it can be transported over the bed by the liquid shear flow. Also the horizontal force component could be critical for bed mobilization, specifically if the sphere-sphere contacts are frictional. Then—as the inset in the top panel of Figure 17 suggests—the horizontal force provides a torque

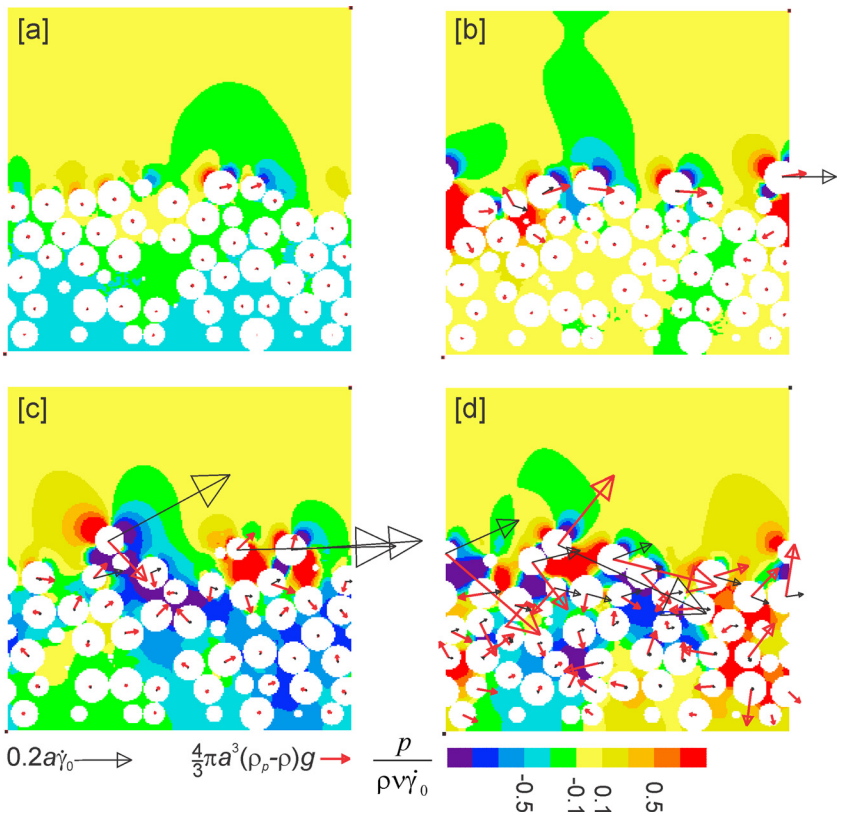

FIG. 16. (Color online) Cross sections through the granular beds; single realizations of the pressure distribution in the liquid along with sphere velocities (black, thin-lined vectors) and hydrodynamic forces on the spheres (red, thick-lined vectors). [a]: $\theta = 0.10$; [b]: $\theta = 0.20$; [c]: $\theta = 0.42$; [d]: $\theta = 0.64$. Re = 0.12–0.13 in all cases.

with respect to a sphere-sphere contact that makes one sphere roll over an underlying one, slightly lifting the moving sphere at the same time.

The probability density functions of the hydrodynamic vertical force and the horizontal, streamwise force on the spheres in the top layer in the beds are given in Figure 17. These are time and space-averaged functions: averaging over the two homogeneous directions and over time during a stationary time interval of $100\frac{a^2}{\nu}$. The streamwise (x) component PDFs are clearly skewed towards positive values which should be given the shear flow in positive x-direction; strong negative x-forces are not exceptional though. Also the vertical forces have a skewness towards the positive (is upwards), specifically noticeable for the lower Shields numbers. This is due to the inertial Saffman lift force experienced by the spheres. A low-Reynolds number expression for lift on a single sphere attached to a flat wall in shear flow is[9] $F_{hz} = 9.22\rho\dot{\gamma}_0^2 a^4$, so that $\frac{F_{hz}}{\frac{4}{3}\pi a^3(\rho_p-\rho)g} = 4.40\theta\mathrm{Re}$. With $\mathrm{Re} = 0.12$ in Figure 17, the lift force becomes 0.5θ which is of the same order of magnitude as the averages of the vertical force PDFs. The root-mean-square values of the z-force are, however, one to two orders of magnitude larger and thus much more relevant quantities for mobilization of the spheres in the bed.

From the PDFs in Figure 17 the probability of a sphere in the top layer feeling a dimensionless force larger than unity has been derived. For the vertical force this implies the probability of a sphere feeling a vertical hydrodynamic force that overcomes its net gravity. For the streamwise force component it would be a measure of the probability of a sphere being able to roll over a neighboring sphere. Probabilities of $\frac{F_h}{\frac{4}{3}\pi a^3(\rho_p-\rho)g} \equiv F_h^*$ being larger than unity as a function of θ are given in Figure 18. For the low θ end of these data there is resemblance with the results in Figure 14 on solids flux that we used for identifying the θ-interval in which incipient solids motion occurs. Specifically the chance of $F_{hz}^* > 1$ is practically zero for $\theta \leq 0.1$ and gets significant for $\theta \geq 0.15$. The horizontal force probability gets non-zero for $\theta \geq 0.1$. Therefore the horizontal force exceeding net gravity is tentatively less critical for the onset of bed mobility.

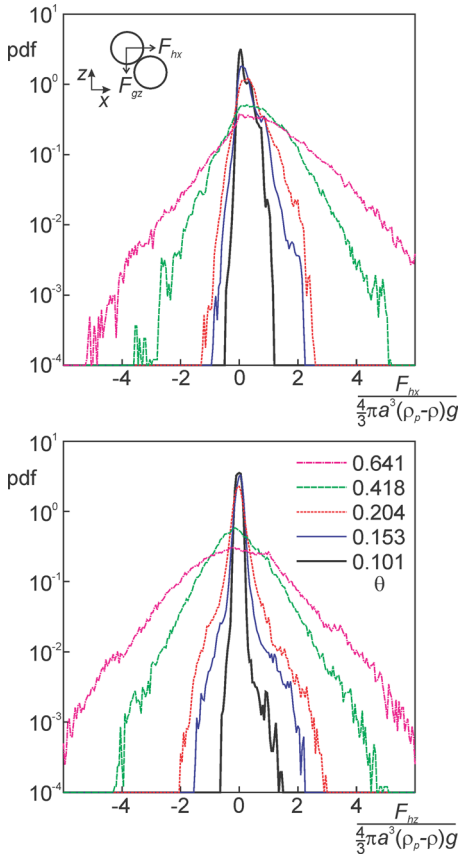

FIG. 17. (Color online) Probability density functions of the resolved hydrodynamic force on the top layer of spheres in the beds for various Shields numbers as indicated. $\mathrm{Re} = 0.12-0.13$. Top: force in streamwise (x) direction; bottom: force in vertical (z) direction.

V. SUMMARY AND CONCLUSIONS

We studied erosion of beds of fine particles supported by a flat bottom wall as a result of a fluid flow. The flow over the bed was a laminar simple shear flow, driven by moving an opposing flat wall. The Reynolds number based on the particle radius and the overall shear rate was in the range 0.02 to 0.6. Bed erosion is largely governed by the competition between gravity and viscous hydrodynamic forces. This is reflected in the definition of the Shields number as an order of magnitude estimate of the ratio of these two forces: $\theta \equiv \frac{\rho\nu\dot{\gamma}}{g(\rho_s-\rho)2a}$. For laminar flow, onset of bed erosion occurs beyond a critical Shields number of approximately 0.15.[5,6]

In this paper, simulations were described that to a large extent resolve the phenomena occurring during bed erosion for relatively simple systems: beds of monosized, spherical particles that only interact through hard-sphere collisions (no other direct sphere-sphere interaction potentials) and through the interstitial liquid. Modeling enters the simulations through lubrication forces and through the friction coefficient. Regarding lubrication forces: The numerical procedure (the lattice-Boltzmann method) uses a fixed grid so that the hydrodynamic interaction between very closely spaced solid surfaces is not resolved. This is compensated for by explicitly adding lubrication forces (based on analytical expressions) to the equations of motion of the spheres. In the same spirit the (dry) friction coefficient accounts for (unresolved)

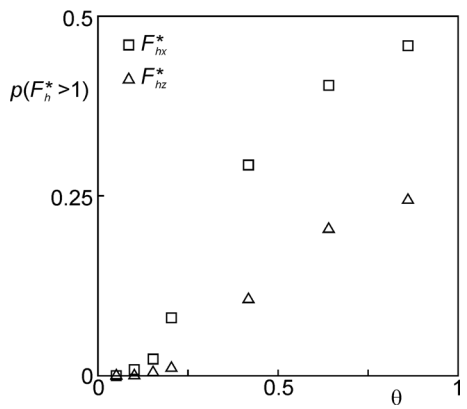

FIG. 18. Probability of $F_h^* \equiv \frac{F_h}{\frac{4}{3}\pi a^3(\rho_p-\rho)g}$ on top layer spheres being larger than 1 as a function of the Shields number. $\mathrm{Re} = 0.12-0.13$.

surface roughness of the spheres. The sensitivity of the global bed dynamics with respect to these modeling steps was assessed. A little friction ($\mu = 0.1$) was sufficient to suppress unphysically strong rotation of solids deep in the bed. Solids mobility was significantly reduced if lubrication forces were active which was expected. Solids mobility was not sensitive with respect to modeling settings of the lubrication force.

In the simulations, the onset of bed erosion occurred between a Shields number of 0.10 and 0.15 which is in line with experimental observations. The Reynolds number and the density ratio were not of influence on the interval containing the critical Shields number. It was argued that—since the critical Shields number does not depend on the Reynolds number—reversible viscous forces, not irreversible inertial (lift) forces are responsible for incipient erosion. For Shields numbers much higher than the critical value the Reynolds number has profound influence on the bed dynamics and the extent to which the flow is able to mobilize and transport solids.

Analysis of the simulation data showed that erosion sets in once the probability of a sphere feeling a vertical hydrodynamic force larger than its own net weight becomes nonzero. At that stage probabilities of horizontal hydrodynamic forces larger than the net weight are already significant.

[1]F. Charru, H. Mouilleron, and O. Eiff, "Erosion and deposition of particles on a bed sheared by a viscous flow," J. Fluid Mech. **519**, 55 (2004).
[2]F. Charru, E. Larrieu, J.-B. Dupont, and F. Zenit, "Motion of a particle near a rough wall in a viscous shear flow," J. Fluid Mech. **570**, 431 (2007).
[3]A. E. Lobkovsky, A. V. Orpe, R. Molloy, A. Kudrolli, and D. H. Rothman, "Erosion of a granular bed driven by laminar fluid flow," J. Fluid Mech. **605**, 47 (2008).
[4]H. Mouilleron, F. Charru, and O. Eiff, "Inside the moving layer of a sheared granular bed," J. Fluid Mech. **628**, 229 (2009).
[5]M. Ouriemi, P. Aussillous, M. Medale, Y. Peysson, and E. Guazzelli, "Determination of the critical Shields number for particle erosion in laminar flow," Phys. Fluids **19**, 061706 (2007).
[6]T. Loiseleux, Ph. Gondret, M. Rabaud, and D. Doppler, "Onset of erosion and avalanche for an inclined granular bed sheared by a continuous laminar flow," Phys. Fluids **17**, 103304 (2005).
[7]J. M. Buffington and D. R. Montgomery, "A systematic analysis of eight decades of incipient motion studies, with special reference to gravel-bedded rivers," Water Resour. Res. **33**, 1993, doi:10.1029/96WR03190 (1997).
[8]D. Paphitis, "Sediment movement under unidirectional flows: An assessment of empirical threshold curves," Coastal Eng. **43**, 227 (2001).
[9]D. Leighton and A. Acrivos, "The lift on a sphere touching a plane wall in the presence of a simple shear flow," J. Appl. Math. Phys. **36**, 174 (1985).
[10]J. J. Derksen and R. A. Larsen, "Drag and lift forces on random assemblies of wall-attached spheres in low-Reynolds number shear flow," J. Fluid Mech. **673**, 548 (2011).
[11]S. Chen and G. D. Doolen, "Lattice–Boltzmann method for fluid flows," Annu. Rev. Fluid Mech. **30**, 329 (1998).
[12]S. Succi, *The Lattice Boltzmann Equation for Fluid Dynamics and Beyond* (Clarondon, Oxford, 2001).
[13]D. Goldstein, R. Handler, and L. Sirovich, "Modeling a no-slip flow boundary with an external force field," J. Comp. Physiol. **105**, 354 (1993).
[14]J. Derksen and H. E. A. Van den Akker, "Large-eddy simulations on the flow driven by a Rushton turbine," AIChE J. **45**, 209 (1999).
[15]E. Papista, D. Dimitrakis, and S. G. Yiantsios, "Direct numerical simulation of incipient sediment motion and hydraulic conveying," Ind. Eng. Chem. Res. **50**, 630 (2011).
[16]S. Kim and S. J. Karrila, *Microhydrodynamics: Principles and Selected Applications* (Butterworth-Heinemann, Boston, 1991).
[17]Y. Yamamoto, M. Potthoff, T. Tanaka, T. Kajishima, and Y. Tsuji, "Large-eddy simulation of turbulent gas-particle flow in a vertical channel: effect of considering inter-particle collisions," J. Fluid Mech. **442**, 303 (2001).
[18]J. J. Derksen and S. Sundaresan, "Direct numerical simulations of dense suspensions: Wave instabilities in liquid-fluidized beds," J. Fluid Mech. **587**, 303 (2007).
[19]J. A. Somers, "Direct simulation of fluid flow with cellular automata and the lattice-Boltzmann equation," Appl. Sci. Res. **51**, 127 (1993).
[20]J. G. M. Eggels and J. A. Somers, "Numerical simulation of free convective flow using the lattice-Boltzmann scheme," Int. J. Heat Fluid Flow **16**, 357 (1995).
[21]A. Ten Cate, C. H. Nieuwstad, J. J. Derksen, and H. E. A. Van den Akker, "PIV experiments and lattice-Boltzmann simulations on a single sphere settling under gravity," Phys. Fluids **14**, 4012 (2002).
[22]P. Duru, M. Nicolas, J. Hinch, and E. Guazelli, "Constitutive laws in liquid-fluidized beds," J. Fluid Mech. **452**, 371 (2002).
[23]P. Duru and E. Guazelli, "Experimental investigations on the secondary instability of liquid-fluidized beds and the formation of bubbles," J. Fluid Mech. **470**, 359 (2002).
[24]A. J. C. Ladd, "Numerical simulations of particle suspensions via a discretized Boltzmann equation. Part 2. Numerical results," J. Fluid Mech. **271**, 311 (1994).
[25]A. S. Sangani and A. Acrivos, "Slow flow through a periodic array of spheres," Int. J. Multiphase Flow **8**, 343 (1982).
[26]H. Hasimoto, "On the periodic fundamental solutions of the Stokes equations and their application to viscous flow past a cubic array of spheres," J. Fluid Mech. **5**, 317 (1959).
[27]J. J. Derksen, "Flow-induced forces in sphere doublets," J. Fluid Mech. **608**, 337 (2008).
[28]J. J. Derksen, "Drag on random assemblies of spheres in shear-thinning and thixotropic liquids," Phys. Fluids **21**, 083302 (2009).
[29]N.-Q. Nguyen and A. J. C. Ladd, "Lubrication corrections for lattice-Boltzmann simulations of particle suspensions," Phys. Rev. E **66**, 046708 (2002).
[30]R. A. Bagnold, "The flow of cohensionless grains in fluids," Philos. Trans. R. Soc. London, Ser. A **249**, 235 (1956).
[31]S. J. White, "Plane bed thresholds of fine grained sediment," Nature **228**, 152 (1970).